A Storm-Permitting Climate Model Reveals the Role of Storm Frequency in Future Changes in Extreme Sea Levels on the US East and Gulf Coasts

Gaopeng Xu[1], Ping Chang[1,2], Gokhan Danabasoglu[3], Frederic S. Castruccio[3], Stephen Yeager[3], Qiuying Zhang[1], Jaison Kurian[1], Justin Small[3], Susan Bates[4], Christine C. Shepard[5]

[1]Department of Oceanography, Texas A&M University, College Station, Texas, USA

[2]Department of Atmospheric Sciences, Texas A&M University, College Station, Texas, USA

[3]NSF National Center for Atmospheric Research, Boulder, Colorado, USA

[4]The Nature Conservancy, Nassawadox, Virginia, USA

[5]The Nature Conservancy, Gulf of Mexico Program, Key West, Florida, USA

Corresponding author: Gaopeng Xu (gaopxu@tamu.edu); Ping Chang (ping@tamu.edu)

Abstract

Storm-induced coastal extreme sea levels (ESLs) pose severe threats to infrastructure, economies, and ecosystems. However, projecting future ESL changes is hindered by the coarse resolution of climate models used in assessment reports, which fail to accurately capture tropical cyclones (TCs) and nor'easters. Here, we demonstrate that high-resolution Community Earth System Model (CESM) simulations realistically reproduce wind- and pressure-induced daily mean extreme dynamic sea levels (DSLs), including the most catastrophic events. Under a high-emission scenario, we show that 50-year return DSLs (DSL50) decrease on the U.S. Texas and Northeast coasts but increase on the U.S. Louisiana and Southeast coasts, creating substantial spatial discrepancies between total DSL50 changes and mean DSL rise. On the Gulf and Southeast coasts, DSL50 trends are primarily driven by TC frequency changes, while nor'easter frequency changes tend to govern trends on the Northeast coast. These findings challenge the traditional assumption of stationarity

in storm-induced ESLs, underscore the importance of high-resolution climate models for regional coastal risk assessment, and represent a critical step toward more accurate projections of future ESLs in a warming climate.

1. Introduction

Storm-induced coastal extreme sea levels (ESLs) pose significant threats to infrastructure, including ports, power plants, and transportation networks, resulting in annual economic losses of tens of billions of dollars[1–3]. As mean sea levels continue to rise, more people will be exposed to coastal floods[2,4], with potential damages ranging from US$21 to 210 trillion by 2100[4,5]. Coastal ecosystems are also increasingly vulnerable to erosion and saltwater intrusion into groundwater[6–12]. These escalating risks highlight the urgent need for coastal communities to better understand and project ESLs to inform adaptation strategies and mitigate future socio-economic losses.

While mean sea level rise is widely recognized as the primary driver of ESL changes[13,14], the influence of storm changes remains uncertain due to the challenges in projecting future storminess[15–18]. Although climate models are used to project mean sea level rise in the Intergovernmental Panel on Climate Change (IPCC) reports, their spatial resolutions are typically around 100 km, which limits their ability to accurately capture storm dynamics and detailed coastal geometry — both crucial for accurate ESL simulations[19]. As a result, two alternatives are often used: (i) probabilistic models, which assume that the statistical properties of storm-induced ESLs are stationary in time and offset the distribution with sea level rise[20–25]; and (ii) regional or global storm surge models, forced by synthetic tropical cyclones (TCs)[26,27] or simulated atmospheric fields from coarse-resolution climate models[28–30]. However, these

methods tend to neglect or underestimate storm characteristic changes, leaving the role of storminess changes in future ESL projections uncertain.

Traditionally, ESLs have been treated as a stationary process and analyzed using return frequencies via extreme value theory (EVT)[31]. However, this assumption is invalidated by ongoing changes in mean sea level and storminess. Nonstationary EVT methods have been introduced to adjust the median and width of generalized extreme value (GEV) distributions using sea level statistics or other climate indicators[20,32–36], but they still fail to fully account for storm changes. Observational studies show that storm-induced ESL trends in Europe have been comparable to mean sea level trends since 1960[37]. Recent advances in modeling and computing now enable the assessment of storm change impacts on ESL nonstationarity using high-resolution climate models. Increasing atmospheric resolution to 25-50 km improves the simulation of tropical and extra-tropical cyclone intensity and tracks[38,39], making it possible to simulate storm-induced ESLs more realistically[40] (Xu et al., 2024). However, global high-resolution climate simulations remain computationally expensive, limiting ensemble sizes and making it difficult to separate natural variability from anthropogenic impacts on ESLs.

In this study, we investigate future storm-induced ESLs on the U.S. Atlantic and Gulf of Mexico coasts using a 10-member ensemble of high-resolution Community Earth System Model (HR CESM) simulations[41–45] (Chang et al., 2025, see **Methods**). We analyze daily mean dynamic sea level (DSL), which represents sea-level departures from the global mean, to assess ESLs without tidal influences. To isolate storm-induced changes from interannual variability and mean sea level rise, we remove the annual mean DSL for each individual year. Our analysis begins by validating the model against observational data, followed by an investigation of projected changes in the 50-year return DSL (DSL50) and its relationship with storm activity.

2. Results

2.1 Comparison with observations

We first evaluate the ability of HR CESM to simulate catastrophic DSLs by comparing its output with tide gauge (TG) observations (see **Methods**) on the U.S. Atlantic and Gulf of Mexico coasts. After removing the annual mean sea level, the largest daily mean DSL event observed at each TG station exhibits a complex spatial pattern along the Atlantic and Gulf coasts (Figure 1a), with most amplitudes ranging from 100 to 160 cm (Figure 1b). The event with the largest amplitude occurred in Galveston, where the daily mean DSL reaches 222 cm. In contrast, stations at Portland, Wilmington, Charleston, and Key West recorded relatively weak DSL events with amplitudes below 100 cm. Among all the stations, Key West shows the lowest value of all the strongest DSL events at just 50 cm (Figure 1b, Extended Figure 1a).

The largest DSLs from the 10-member HR CESM ensemble show good agreement with TG observations (Figure 1b), with a root-mean-square error (RMSE, see **Methods**) of 33 cm — approximately 28% of the station-mean observed maximum DSL—and a spatial correlation coefficient of 0.85. The ensemble mean of the maximum DSLs in all realizations also performs well, with an RMSE of 23 cm (about 20% of the observed station mean) and a spatial correlation coefficient of 0.77. These results demonstrate that HR CESM ensemble effectively captures both the magnitude and spatial variability of the largest daily mean DSLs observed on the Atlantic and Gulf coasts. However, intra-ensemble variability is particularly large at Galveston, leading to a RMSE of 92 cm (Extended Figure 1b). While the observed maximum DSL (222 cm) is reasonably reproduced by 2 of the 10 ensemble members, the remaining 8 members underestimate it by 20-70% (Figure 1b). In contrast, at the other 14 TG stations, the intra-ensemble variability is smaller, with an average RMSE of 14 cm on the Northeast coast (from

Portland, Maine to Sewells Point, Virginia) and 23 cm on the Southeast and Gulf coasts (Extended Figure 1b). Additionally, on the Southeast and Gulf coasts, the observed events and majority of simulated events in HR CESM occur during the hurricane season, particularly between September and November (Figure 1c). In contrast, on the Northeast coast, the strongest events are predominantly linked to winter storms between November and April. However, at Baltimore and Wilmington, extreme events were caused by Hurricane Isabel (September 2003) and Hurricane Florence (September 2018), respectively. These September-October TC events are captured by only one or two HR CESM realizations at each station, while the remaining ensemble members attribute the extremes to winter storms.

During storm events, both sea level pressure (SLP) and surface winds drive sea level surges. The former, known as the inverse barometer effect (IBE, **see Methods**), causes sea levels to rise by approximately 1 cm for every 1 hPa drop in SLP[46]. On the Atlantic and Gulf coasts, DSLs induced by wind and pressure forcing are nearly indistinguishable between HR CESM and TG observations (Figure 1d, e, f), indicating that the model realistically simulates not only the largest DSLs but also other storm-induced events and the relative contributions of surface winds and SLP to total DSL. Wind-driven DSLs exhibit a strong linear correlation with the total DSLs with R^2 values ranging from 0.85 to 0.89, indicating that 85%-90% of the total DSL variability is explained by wind forcing (Figure 1d, e, f). In contrast, SLP-induced DSLs show a weaker correlation, with R^2 values below 0.3, indicating a smaller influence of IBE on overall DSL variability. The steeper slope of the wind-induced DSL fit further demonstrates that surface winds are the dominant driver of extreme DSLs, while SLP-induced effects play a secondary role. These results highlight the importance of accurately representing surface wind forcing in climate models, as it significantly outweighs pressure effects in driving extreme DSL events.

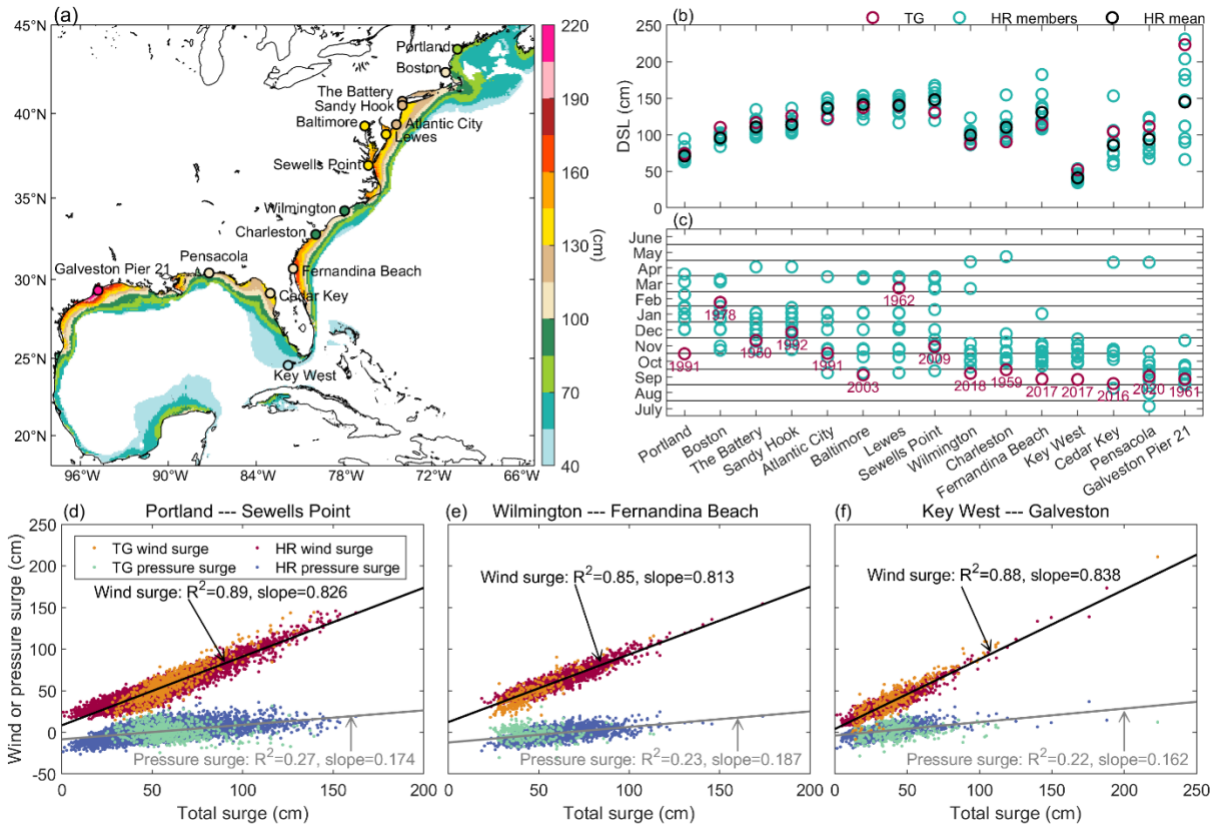

Figure 1 Comparison of observed and simulated extreme DSLs from 1920 to 2020. (a) Spatial distribution of the largest DSLs in TG observations (circles) and the 10-member HR CESM ensemble (shading). **(b)** Amplitudes of the largest DSLs at TG stations (rose red), individual HR CESM ensemble members (green) and the ensemble mean (black). **(c)** Month of occurrence for the largest DSLs in TG observations (rose red) and 10 HR CESM ensemble members (green). The numbers indicate the year of the largest DSLs in TG observations. For each TG station, the largest DSL in HR CESM is defined as the largest value within a 1° radius of the station. Contributions of wind- and pressure-induced DSL surge to total DSL surges in TG observations and HR CESM on the **(d)** Northeast (from Portland to Sewells Point), **(e)** Southeast (from Wilmington to Fernandina Beach), and **(f)** Gulf (from Key West to Galveston) coasts. Orange dots represent TG wind surges, rose red dots show HR CESM wind surges, green dots

indicate TG pressure surges, and blue dots depict HR CESM pressure surges. Regression is performed using both TG and HR CESM data. Data used in (d-f) is from 1940-2020 because SLP from ERA5 is only available to calculated observed IBE during this period.

2.2 Changes in extreme sea level

DSL50 represents the magnitude of a DSL event that has a 1-in-50 chance of being exceeded in any given year. A companion study (Xu et al., 2025) shows that HR CESM realistically captures DSL50 when compared to TG observations. Here, we use the GEV distribution to estimate DSL50 (see **Methods**) based on annual maximum of daily mean DSL and assess its future changes. DSL50 is generally higher on the Atlantic coast (100-120 cm) compared to the Gulf coast (~70 cm, Figure 2a), indicating a heavier right tail in the extreme DSL distribution on the Atlantic coast. This suggests that the Atlantic coast is more frequently impacted by storms than the Gulf coast. However, in each subregion, the spatial variability of DSL50 closely resembles that of the largest DSLs. For instance, on the Gulf coast, both metrics exhibit local peaks on the Texas, Louisiana, and Florida coasts. Our results show that DSL50 is primarily driven by wind forcing (Figure 2b), with a spatial correlation coefficient of 0.91, while contributions from SLP are relatively minor, accounting for less than 18% of total DSL50 (Figure 2c). Notably, SLP-induced DSL50 is particularly large on the Louisiana, North Carolina, and Virginia coasts, suggesting a higher frequency of low-pressure weather systems in these regions[47].

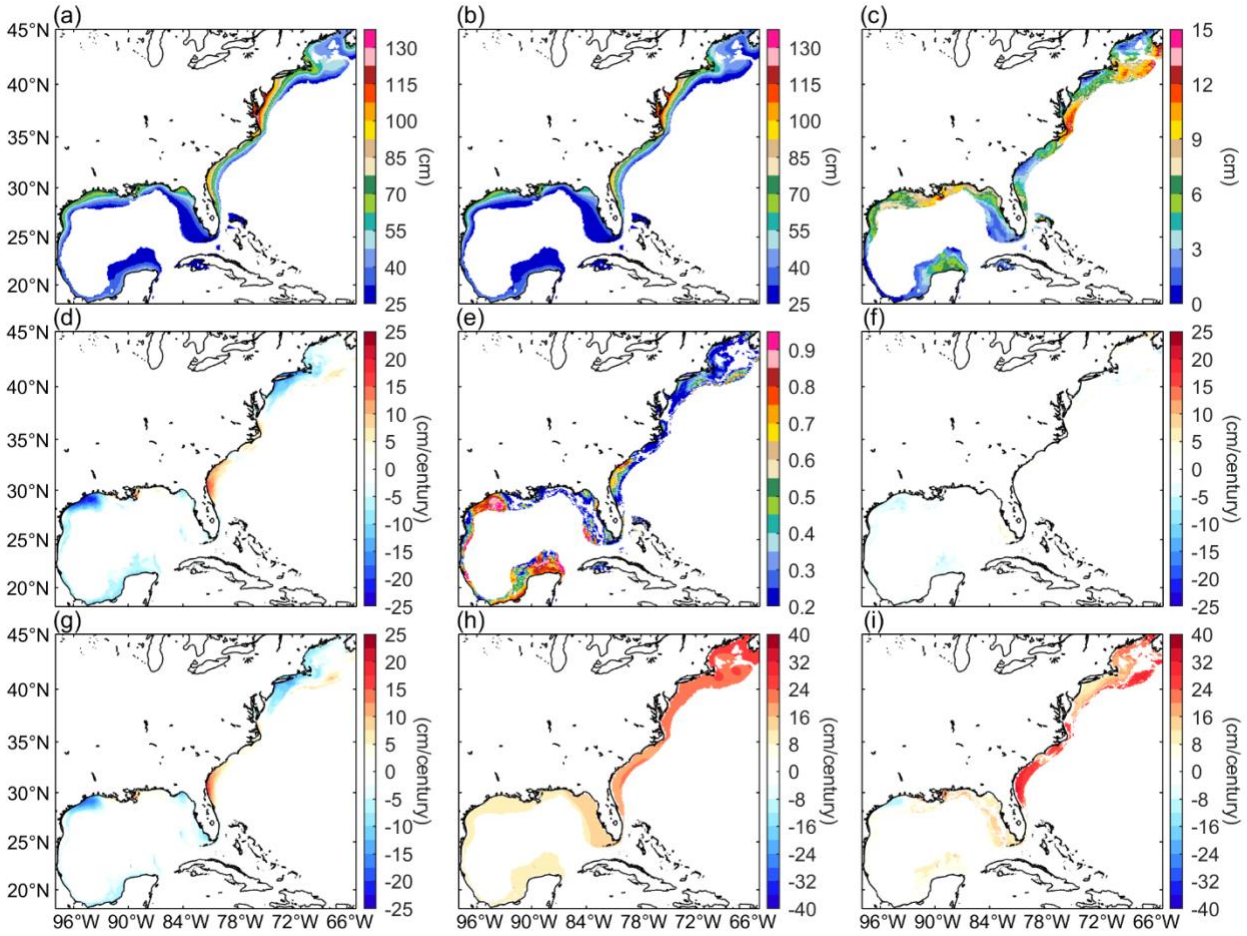

Figure 2 DSL50 during 2006-2035 and its projected trend from 2006 to 2100. (a) Total, **(b)** wind-induced, **(c)** pressure-induced DSL50 in 2006-2035 in HR CESM. Note that the color bar scale for panel (c) is much smaller than those of panels (a) and (b). **(d)** Long-term trends in total DSL50 from 2006 to 2100. **(e)** R^2 values of the linear trends in total DSL50. **(f, g)** Trends in (f) pressure-induced, and (g) wind-induced DSL50. **(h)** Multi-model ensemble mean trend in annual DSL. **(i)** Sum of the trends in total DSL50 in HR CESM and multi-model ensemble mean DSL. All trends are calculated over the period 2006-2100. Trends are all significant at 95% confidence level.

The DSL50 trend from 2006 to 2100 exhibits a complex spatial pattern, with significant decreases on the Texas and Northeast coasts and increases on the Louisiana and Southeast coasts

at the 95% confidence level (Figure 2d). The strongest decrease, −24.5 cm per century, occurs along the Texas coast, while the largest increase, +19.2 cm per century, is observed along the east coast of Florida. The R^2 for these linear trends varies spatially, reaching 0.8–0.9 on the Texas coast, indicating a strong dominance of the linear trend. The Southeast coast follows with R^2 values of 0.7–0.8, while the Northeast and New Orleans coasts show values ≤0.4 (Figure 2e). The decomposition of the DSL50 trends reveals that SLP contributes less than 6 cm per century to the total change in most regions. This SLP-driven trend is negative along the Texas coast but positive along the Florida and Atlantic coasts (Figure 2f), indicating regionally contrasting changes in storm-related SLP. The negative (positive) trends suggest that storm-related SLP is projected to weaken (intensify), which is closely linked to changes in storm strength. However, the relationship between minimum storm-induced SLP and IBE requires further investigation, which is beyond the scope of this study. In contrast to SLP, wind forcing emerges as the primary driver of the overall DSL50 trend (Figure 2g). To verify the robustness of these trends, we perform a leave-one-out analysis by recalculating the wind-induced DSL50 trends using 9 out of 10 ensemble members, resulting in 10 combinations. The mean of these combinations exhibits a similar spatial pattern of DSL50 trends to that directly obtained from the 10 ensemble members (Extended Figure 2, Figure 2e).

The amplitude of DSL50 trends is comparable to that of projected mean sea level rise. Among the CMIP6 models, four include ocean simulations at approximately 25 km resolution spanning 1850 to 2100 (CNRM-CM6-1-HR, EC-Earth3P-HR, HadGEM3-GC31-MM, and GFDL-CM4). However, these models only provide monthly DSL output, rather than daily data, which makes it impossible to directly calculate DSL50. Nevertheless, they can still be used to estimate the multi-model ensemble mean of projected coastal mean DSL rise from 2006 to 2100, in combination

with HR CESM (Figure 2h). The strongest mean DSL rise occurs on the Northeast coast, followed by the Southeast and Gulf coasts. Most previous studies assume mean DSL rise to be the dominant driver of future changes in extreme DSLs, with changes in storm statistics playing a minor role[20–25]. However, our results indicate that storm-induced DSL50 changes are comparable in magnitude to mean DSL rise. As a result, the total extreme DSL trend, defined as the sum of trends in DSL50 and mean DSL, reaches its maximum on the Southeast coast rather than the Northeast coast, particularly on the east Florida coast (Figure 2i). For example, overlooking the influence of storminess can lead to an underestimation of DSL50 trends by up to 48% at Fernandina Beach. This may have profound implications for coastal adaptation strategies, especially at the national level, as it challenges the conventional assumption that mean DSL rise is the primary driver of future extreme DSL changes. Because wind forcing is the dominant driver of DSL50 trends, the following analysis focuses on wind-induced DSL50 changes.

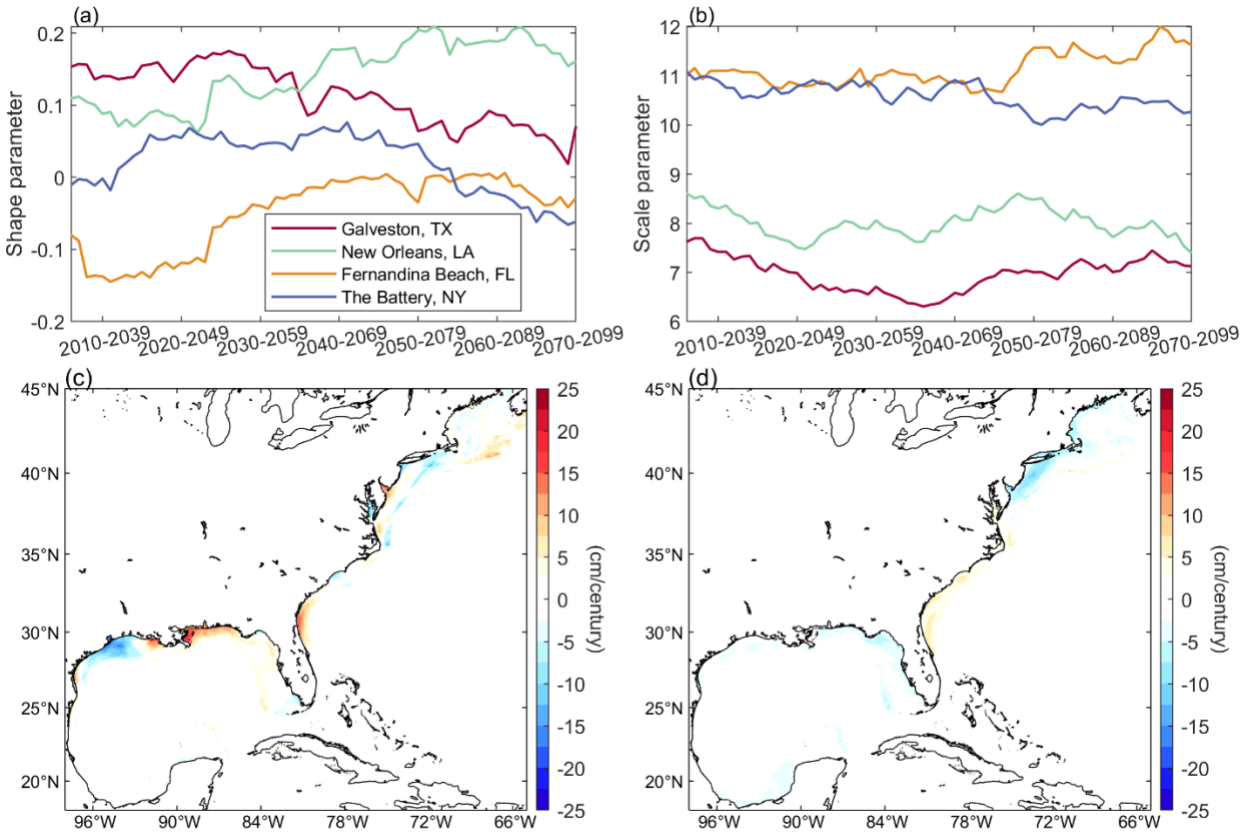

Figure 3 Contributions of GEV parameters to wind-induced DSL50 trends. (a, b) Time series of (a) shape and (b) scale parameters of GEV distributions. **(c)** Contributions of the shape parameter to the wind-induced DSL50 trend. **(d)** Same as (c) but for the scale parameter.

Prior research has commonly attributed changes in extreme DSLs primarily to changes in mean DSL, with assumption that the width and shape of DSL GEV distribution remaining constant over time[25,48,22,21] or being parameterized using climate indicators[32]. To evaluate this assumption, we analyze the time series of the shape and scale parameters from the GEV distribution at four representative tide gauge stations—Galveston (Texas coast), New Orleans (Louisiana coast), Fernandina Beach (Southeast coast), and The Battery (Northeast coast)—where DSL50 exhibits significant trends (Figure 3a, b). A positive (negative) shape parameter value indicates a right (left) tailed GEV distribution while the scale parameter measures the width of the distribution.

Therefore, a larger shape parameter value corresponds to a longer right tail of the GEV distribution. Our results reveal that both parameters vary nonmonotonically over time, challenging the assumption of constant storm characteristics. The shape parameter is projected to decrease at Galveston and The Battery, suggesting a shorter right tail and thus weaker DSL extremes in the future. In contrast, the parameter value is projected to increase at New Orleans and Fernandina Beach, indicating a longer right tail and stronger DSL extremes. The scale parameter also exhibits regional contrasts. At The Battery, it is projected to decrease after 2040, indicating a narrower GEV distribution, which, combined with the decreasing shape parameter, weakens future DSL50. In contrast, at Fernandina Beach, the scale parameter is projected to increase, resulting in a wider GEV distribution that enhances DSL50, consistent with the increasing shape parameter. At Galveston and New Orleans, the scale parameter shows only a slight decrease, despite substantial internal variability. Results remain the same when using 9 of 10 ensemble members (Extended Figure 3a, b), suggesting that our results are not sensitive to the sample size. Overall, DSL50 aligns more strongly with the shape parameter than the scale parameter at all four stations (Extended Figure 3c, d). The correlation between DSL50 and the shape parameter exceeds 0.85 at all locations, reaching a maximum of 0.95 at Fernandina Beach. In contrast, the maximum correlation between DSL50 and the scale parameter is only 0.65 at The Battery, with the lowest correlation of 0.28 at Galveston. To quantify the relative importance of the shape and scale parameter in driving DSL50 trends, we isolate the influence of each parameter when calculating DSL50 trends (see **Methods,** Figure 3c, d). The results indicate that: (i) on the Gulf coast, DSL50 trends are primarily driven by the change in the shape parameter; (ii) on the Northeast coast, the change in the scale parameter dominates the DSL50 trend; (iii) on the Southeast coast, changes in both parameters contribute, although the shape parameter change

plays a larger role. Because the annual mean DSL is removed when calculating DSL50, the influence of the location parameter is negligible compared to the other two parameters (Extended Figure 3e). These findings highlight the importance of accounting for changes in both shape and scale parameters when using probabilistic methods to project future ESL changes. Additionally, accurately parameterizing these two parameters under a warming climate remains a challenge due to their nonlinear and spatially variable behavior. In the following section, we investigate the physical drivers of DSL50 changes.

2.3 Role of storms in extreme sea level changes

Since the seasonal cycle of DSL is retained in the DSL50 calculation, we next assess its role in DSL50 trends. At Galveston, New Orleans, and Fernandina Beach, the seasonal cycle of DSL50 (see **Methods**) from 2006 to 2035 is well-aligned with the DSL seasonal cycle, both peaking in October (Extended Figure 4 a, c, e). In contrast, strong DSL50 events at The Battery primarily occur during winter season (i.e., nor'easter season), while the DSL seasonal cycle peaks in October (Extended Figure 4g). This timing mismatch reduces the seasonal influence on DSL50 trends, a phenomenon also noted in a previous study[49]. However, the trends in DSL50 from 2006 to 2100 exhibit substantial discrepancies compared to those of the DSL seasonal cycle at all four stations. At New Orleans and Fernandina Beach, DSL50 shows peak increases in November—10 cm and 20 cm per century, respectively—exceeding trends in the DSL seasonal cycle (Extended Figure 4 d, f). Similarly, the strongest DSL50 decreases occur in September at Galveston and in April at The Battery, also outpacing corresponding DSL cycle trends (Extended Figure 4 b, h). These results suggest that changes in the DSL seasonal cycle have only a minor influence on DSL50 trends along the Atlantic and Gulf coasts.

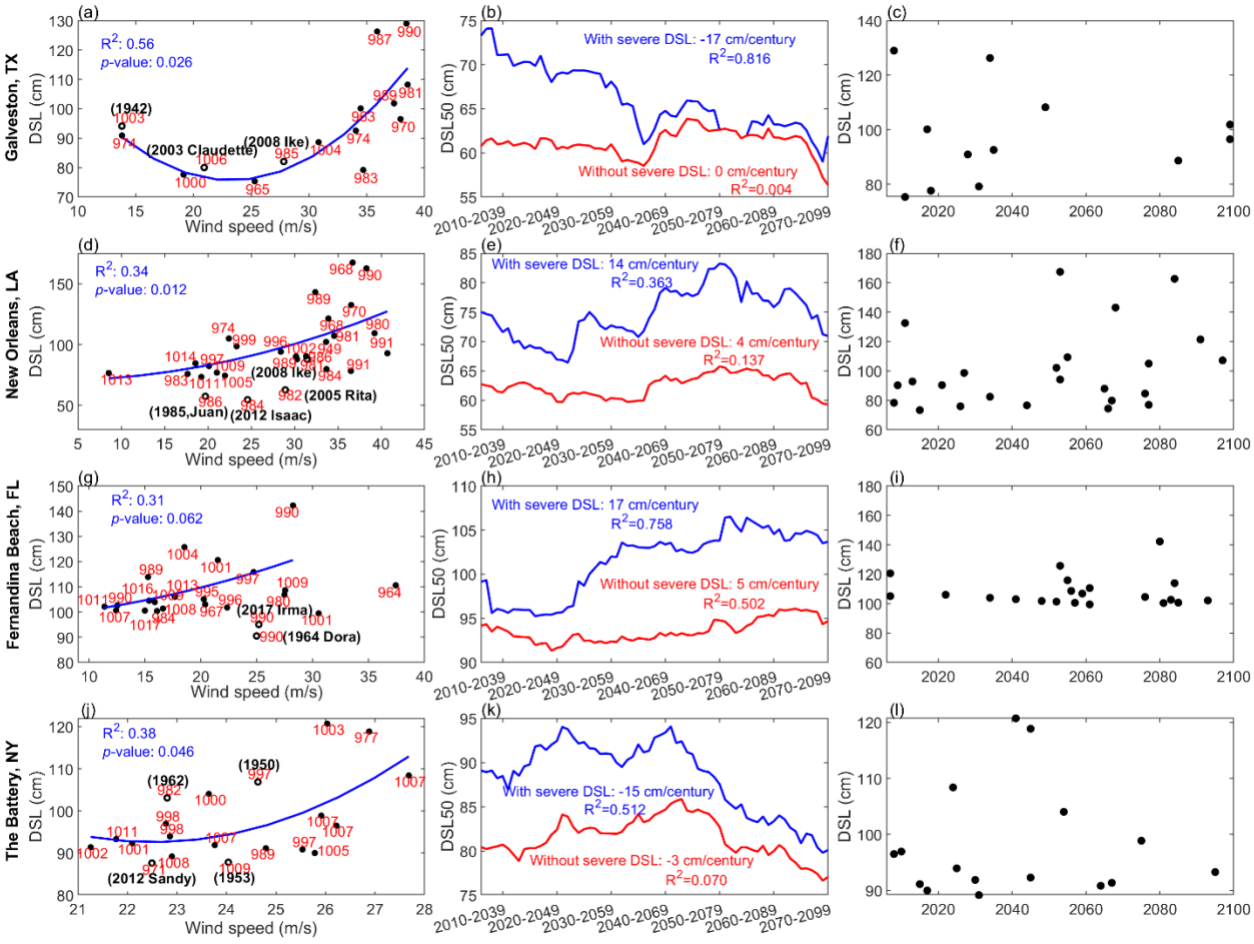

Figure 4 Relationship between storms and severe DSL. (a, d, g, j) Scatterplots of surface wind speed versus DSL at four TG station. Red numbers indicate the minimum SLP in the vicinity of TG stations. Observations, which have similar amplitudes of wind-induced DSL to HR CESM DSL50 during 2006-2035, are shown as open black circles, with event names and years labeled in brackets. Observations at New Orleans are taken from Grand Isle TG station. DSL50 during 2006-2035 is 73.29, 71.33, 99.20, and 89.05 cm at Galveston, New Orleans, Fernandina Beach, and The Battery TG stations, respectively. **(b, e, h, k)** Time series of wind-induced DSL50 with (blue) and without (red) severe DSL events. Linear trends of DSL50 and their R^2 values are labeled in each panel. **(c, f, i, l)** Occurrence time of severe DSL events with y-

axis representing DSL amplitudes. The first, second, third, and fourth rows correspond to results for Galveston, New Orleans, Fernandina Beach, and The Battery, respectively.

A possible key driver of DSL50 trends is storm activity changes, including TCs and nor'easters. To address their impact, we focus on severe DSL events, defined as events where DSL exceeds the DSL50 of the 2006-2035 period. At Galveston, 12 severe events are identified between 2006 and 2100 in 10 ensemble members of HR CESM. These events are linked to TCs with lowest daily mean SLP ranging from 974 hPa to 1004 hPa (Figure 4a and Extended Figure 5). Consistent with previous studies[40,50,51], daily-mean DSL exhibits a quadratic relationship with 6-hourly-mean maximum surface wind speed (see **Methods**), with R^2=0.56 and p=0.026. Notably, historical large DSL surges observed in 1942, 2003, and 2008 align well with the relationship obtained from HR CESM simulations. This relationship can be impacted by TC track, size, intensity, and translation speed[19,52,53]. After excluding these severe events, the DSL50 trend changes from -17 cm to 0 cm per century with R^2 decreased from 0.82 to 0.004 (Figure 4b), suggesting the importance of severe events in DSL50 changes. However, the impact of TCs on DSL50 is stronger in 2006-2060 than in 2060-2100. This is due to a decline in TC occurrence near Galveston, with 9 events occurring from 2006 to 2060 (4 in 2006-2020 and 5 in 2020-2050), but only 3 from 2060 to 2100 (Figure 4c).

24 simulated severe events occur at New Orleans from 2006 to 2100, with daily mean SLP ranging from 970 to 1013 hPa (Figure 4d). Of these, 20 are linked to TCs and 4 to frontal systems (Extended Figure 6). The quadratic regression between daily-mean DSL and 6-hourly surface wind speed yields a R^2 value of 0.34 with a p-value of 0.012. Observed DSL responses to Hurricanes Juan, Rita, Isaac, and Ike are consistent with HR CESM results, though the first three exhibit weaker responses than model-simulated events with similar wind speeds. Excluding these

severe events reduces the DSL50 trend from 14 cm to 4 cm per century. The strongest positive DSL50 trend occurs from 2020 to 2080, coinciding with 13 TCs and 3 frontal events (Extended Figure 6). Among these 16 events, 5 (4 TCs and 1 front event) occur between 2020 and 2050, while 11 (9 TCs and 2 front events) occur between 2050 and 2080, contributing to the increase in DSL50. Notably, there are 9 TC-driven severe events at both Galveston and New Orleans during these two periods. However, their distribution differs: from 2020 to 2050, 5 TCs impact Galveston and 4 affect New Orleans, whereas from 2050 to 2080, all 9 TCs occur in the vicinity of New Orleans. This shift suggests a possible change in TC tracks from Texas toward Louisiana. Further validating this result requires additional multi-model high-resolution climate simulations.

Compared to New Orleans, Fernandina Beach is more frequently impacted by frontal systems, which are responsible for 8 severe DSL events from 2006 to 2100 (Extended Figure 7). Of the remaining severe events, 11 are TC-driven and 2 are linked to nor'easters. Excluding two outlier TC events with wind speeds exceeding 30 m/s, the quadratic correlation between daily-mean DSL and 6-hourly wind speed yields R^2=0.3 and p=0.062, which is consistent with observed DSL response to surface wind (Figure 4g). The two outliers correspond to: a 2007 TC moved from the Gulf of Mexico to the North Atlantic and a 2061 TC moved from the subtropical North Atlantic to the U.S. east coast. Similar to New Orleans, excluding these 21 severe events reduces the DSL50 trend from 17 cm to 5 cm per century (Figure 4h). The strongest influence occurs from 2020 to 2080, during which 4 severe events occur from 2020 to 2050 (only 1 TC-driven) while 8 severe events occur from 2050 to 2080 (5 TC-driven) (Figure 4i). A recent study suggests increased TC activity may result from enhanced vertical wind shear and atmospheric stability[54], highlighting the need for further TC analyses on the Gulf and Southeast coasts. Based

on these findings, we conclude that TC frequency is the primary driver of DSL50 on the Gulf and Southeast coasts.

At The Battery, all 16 severe DSL events are nor'easter-induced, characterized by strong temperature gradients within the low-pressure system at 500 hPa (Extended Figure 8), showing consistency with previous results[55]. Compared to TC-induced events, nor'easter winds are weaker, ranging from 21 to 28 m/s (Figure 4j), yet daily DSL still exhibits a quadratic relationship with 6-hourly wind speeds (R^2=0.38 and p=0.046). Four observed strong DSL surge events scattered around this quadratic relationship, further confirming the realism of HR CESM simulations. Excluding these nor'easter-driven events reduces the DSL50 trend from -15 cm to -3 cm per century, with most of this change occurring after 2040 (Figure 4k). As shown in Figure 4l, there are 6 severe events from 2040 to 2070 but only 2 events from 2070 to 2100, suggesting a decrease in nor'easter frequency near The Battery. This decreasing nor'easter frequency is consistent across multiple climate models[40,56–58] and it is likely driven by a weakened lower-tropospheric meridional temperature gradient, a consequence of polar amplification[58,59].

3. Conclusions

Projecting future changes in coastal ESLs remains challenging, largely due to the coarse resolution of models used in assessment reports, which struggle to accurately represent extreme weather events, such as TCs and nor'easters. However, recent studies have demonstrated that high-resolution climate models can improve simulations of TCs[38], nor'easters[39], and coastal daily mean ESLs (Xu et al., 2025). In this study, we further demonstrated the realism of HR CESM in simulating wind- and pressure-induced DSL events on the U.S. Atlantic and Gulf coasts. Additionally, the amplitudes of the largest DSL events observed at TG stations on the Atlantic and Gulf coasts fall within the ensemble spread of the simulated largest DSL events. We further

investigated projected changes in storm-induced DSLs under a high-emission scenario (RCP8.5). Our results reveal a complex pattern in future DSL50 trends on the Atlantic and Gulf coasts. DSL50 decreases on the Texas and Northeast coasts but increases on the Louisiana and Southeast coasts. These changes are comparable to the projected mean DSL change, which shows a consistent rise along the entire coast, resulting in differences between the spatial patterns of future extreme and mean DSL changes. Furthermore, our findings challenge the stationarity assumption that is commonly used in future projections of future ESL changes using statistical methods. Our physics-based high-resolution model simulations show that the GEV parameters evolve nonlinearly over time, exhibiting significant spatial variability. Neglecting this nonstationarity can lead to an underestimation of DSL50 trends by up to 48% at Fernandina Beach. This underscores the importance of statistical methods that incorporate changes in both mean sea level and storminess when estimating future ESLs. Our analysis highlights that changes in TC frequency are the primary driver of DSL50 trends on the Gulf and Southeast coasts, suggesting an increase in TC frequency near Louisiana and the Southeast coast but a decrease near Texas. In contrast, on the Northeast coast, the decreasing frequency of nor'easters dominates the DSL50 trend.

Despite these advancements, our study has several limitations. One key uncertainty lies in simulating extreme events in the Gulf of Mexico, particularly near Galveston, where the ensemble spread of the largest DSLs remains large, suggesting it is still challenging for HR CESM to project ESLs along Texas coast. Addressing this issue requires a multiple high-resolution modeling approach to improve our understanding of projected storm-ESL interactions. However, current simulations from High-Resolution Model Intercomparison Project (HighResMIP)[60] only extend to 2050. Future efforts could focus on extending high-resolution

simulations to 2100 and incorporating daily mean DSL into HighResMIP2[61] to enhance our understanding of TC-induced DSL changes. Another limitation is that only daily mean DSL is evaluated because it is still challenging for high-resolution climate models to output hourly ocean variables. Additionally, tides' contributions to ESLs are not represented in global climate models and must be diagnosed offline and added to the extreme DSLs simulated by these models. Despite these challenges, this study represents a critical step toward improving future ESL projections. Extreme events captured by high-resolution climate models can further inform machine learning approaches and drive regional models for more targeted ESL assessments. Our findings underscore the importance of region-specific analyses in coastal adaptation and mitigation strategies and highlight the continued need for advancing high-resolution modeling to better capture the risks of extreme coastal flooding.

Methods

HR CESM simulations: The high-resolution simulations are based on CESM version 1.3[42]. The atmospheric component is the Community Atmosphere Model version 5 (CAM5) with the Spectral Element dynamical core. The ocean component is the Parallel Ocean Program version 2 (POP2). The sea-ice component is the Community Ice Code version 4 (CICE4), and the land component is the Community Land Model version 4 (CLM4). The model has a nominal horizontal resolution of 10 km for the ocean and sea ice components, and 25 km for the atmosphere and land components. The simulations include a 500-year preindustrial control (PI-CNTL) and a historical-and-future transient (HF-TNST) climate simulation from 1850-2100. PI-CNTL is forced by a perpetual climate forcing reflecting 1850 conditions, while HF-TNST is branched from PI-CNTL at year 250, using observed climate forcing until 2005, after which it follows the high emission scenario RCP 8.5. Nine additional HF-TNST simulations were

performed, starting in 1920 with slightly different atmospheric initial conditions, resulting in a 10-menber HR HF-TNST ensemble.

Observed sea level by tide gauges: The observational sea levels from 15 TG stations on the U.S. Atlantic and Gulf of Mexico coasts (Figure 1) are obtained from Global Extreme Sea Level Analysis Version 3 dataset[62–64]. These stations were selected based on the availability of over 70 years of data, with each year containing at least 320 days of valid observations. Tides are removed using Utide Matlab functions[65], and corrections for the vertical land motion and barystatic Gravitation, Rotation, and Deformation fingerprints are applied based on estimates provided by Dangendorf et al. (2023)[66]. For a fair comparison with CESM, the global average sea level estimated by Dangendorf et al. (2024)[67] is also removed to obtain DSL.

Root-mean-square error: The root-mean-square error (RMSE) of the simulated strongest DSL (x_i) at each TG station is defined as $RMSE = \sqrt{\frac{\sum_{i=1}^{N}(x_i - X)^2}{N}}$, where X is the observed strongest DSL at the corresponding TG station, and N is the ensemble size of HR CESM (i.e., $N = 10$).

Inverse Barometer Effect (IBE): It is calculated based on $IBE = -\frac{SLP - \overline{SLP}}{\rho_0 g}$, where overbar represents long-term mean from 1940 to 2020, $\rho_0$is the density of sea water taken as 1026 kg/m^3, and g is the acceleration of gravity taken as 9.8 m/s^2. IBE in the observation is estimated using SLP from ERA5[68].

Extreme value analysis: Extreme DSL simulated by CESM is defined as the yearly maximum after removing the annual mean, and is used to fit a Generalized Extreme Value (GEV) distribution[31]. The cumulative distribution function of GEV for a random and independent variable x is given by

$$G(x) = exp\left\{-\left[1 + \xi\left(\frac{x-\mu}{\sigma}\right)\right]^{-1/\xi}\right\},$$

where μ, σ, and ξ are the location, scale, and shape parameters, representing the distribution mean, width, and tail behavior, respectively. The return period for a given DSL (x_p) is calculated as $1/p$, where $p = 1 - G(x \leq x_p)$ is the exceedance probability, i.e., the probability that x_p is exceeded. The 50-year return level is obtained by setting $p = 0.02$. A 30-year running window (advanced by 1 year) is used to compute time series for μ, σ, ξ, and DSL50 from 2006 to 2100. Then the linear DSL50 trend from 2006 to 2100 is calculated at each grid point. The DSL50 seasonal cycle is calculated by fitting the maximum of DSL in each month to the GEV distribution.

Relative importance of parameters in DSL50 changes: To quantify the importance of σ in DSL50 changes, we keep μ and ξ constant at their 2006 values, only allowing σ to vary over time. A similar process is applied to quantify the impact of ξ and μ on DSL50 changes.

6-hourly surface wind index: Because DSL responds nonlinearly to surface wind, its daily mean amplitude is largely influenced by high-frequency extreme wind events. To capture this effect, we construct a high-frequency wind index by first identifying the maximum 6-hourly surface wind speed on the same day as the DSL within a 2.5° radius of each TG station. Among the four available wind speed indices, we select the time step when the wind location is closest to the Galveston, New Orleans, and Fernandina Beach stations. However, because nor'easters have larger spatial scales than TCs, for The Battery station, we instead select the time step when the wind location is farthest from the station.

Data availability

The CESM data used in this work are available from https://project.cgd.ucar.edu/projects/MESACLIP/. The tide gauge data can be downloaded from https://gesla787883612.wordpress.com/downloads/. The SLP from ERA5 can be downloaded from DOI:10.24381/cds.adbb2d47.

Code availability

The CESM codes are available on GitHub (https://github.com/ihesp/CESM_SW).

Acknowledgments

This research was supported by the National Academies of Sciences, Engineering, and Medicine (NASEM) Gulf Research Program grant 2000013283 and the NSF grant AGS-2231237. The NSF National Center for Atmospheric Research (NCAR) is a major facility sponsored by the NSF under Cooperative Agreement 1852977. We acknowledge the Texas Advanced Computing Center at the University of Texas at Austin providing HPC resources on Frontera. We also acknowledge high-performance computing support from Derecho: HPE Cray EX System (https://doi.org/10.5065/qx9a-pg09) provided by the NSF NCAR's Computational and Information Systems Laboratory, sponsored by the NSF.

Author contributions

Conceptualization: PC, GX. Investigation: GX, PC. Simulations: QZ, FC, SY. Analysis: GX. Visualization: GX. Funding acquisition: PC, GD, SB, CS. Writing – original draft: GX. Writing – review & editing: PC, GD, FC, SY, JK, JS, GX.

Competing interests Statement

The authors declare no competing interests.

References

1. Hallegatte, S., Green, C., Nicholls, R. J. & Corfee-Morlot, J. Future flood losses in major coastal cities. *Nat. Clim. Change* **3**, 802–806 (2013).

2. Hanson, S. *et al.* A global ranking of port cities with high exposure to climate extremes. *Clim. Change* **104**, 89–111 (2011).

3. Kron, W. Coasts: the high-risk areas of the world. *Nat. Hazards* **66**, 1363–1382 (2013).

4. Hinkel, J. *et al.* Coastal flood damage and adaptation costs under 21st century sea-level rise. *Proc. Natl. Acad. Sci.* **111**, 3292–3297 (2014).

5. Jevrejeva, S., Jackson, L., Grinsted, A., Lincke, D. & Marzeion, B. Flood damage costs under the sea level rise with warming of 1.5 C and 2 C. *Environ. Res. Lett.* **13**, 074014 (2018).

6. Nicholls, R. J. & Cazenave, A. Sea-level rise and its impact on coastal zones. *science* **328**, 1517–1520 (2010).

7. Lovelock, C. E., Feller, I. C., Reef, R., Hickey, S. & Ball, M. C. Mangrove dieback during fluctuating sea levels. *Sci. Rep.* **7**, 1680 (2017).

8. Li, G., Törnqvist, T. E. & Dangendorf, S. Real-world time-travel experiment shows ecosystem collapse due to anthropogenic climate change. *Nat. Commun.* **15**, 1226 (2024).

9. Ury, E. A., Yang, X., Wright, J. P. & Bernhardt, E. S. Rapid deforestation of a coastal landscape driven by sea-level rise and extreme events. *Ecol. Appl.* **31**, e02339 (2021).

10. Hauser, S., Meixler, M. S. & Laba, M. Quantification of impacts and ecosystem services loss in New Jersey coastal wetlands due to Hurricane Sandy storm surge. *Wetlands* **35**, 1137–1148 (2015).

11. Smith, T. J. *et al.* Cumulative impacts of hurricanes on Florida mangrove ecosystems: sediment deposition, storm surges and vegetation. *Wetlands* **29**, 24–34 (2009).

12. Nordio, G. *et al.* Frequent storm surges affect the groundwater of coastal ecosystems. *Geophys. Res. Lett.* **50**, e2022GL100191 (2023).

13. Ocean, Cryosphere and Sea Level Change. in *Climate Change 2021 – The Physical Science Basis: Working Group I Contribution to the Sixth Assessment Report of the Intergovernmental Panel on Climate Change* (ed. Intergovernmental Panel on Climate Change (IPCC)) 1211–1362 (Cambridge University Press, Cambridge, 2023). doi:10.1017/9781009157896.011.

14. Sun, Q., Dangendorf, S., Wahl, T. & Thompson, P. R. Causes of accelerated High-Tide Flooding in the US since 1950. *Npj Clim. Atmospheric Sci.* **6**, 210 (2023).

15. Knutson, T. R. *et al.* Tropical cyclones and climate change. *Nat. Geosci.* **3**, 157–163 (2010).

16. Roberts, M. J. *et al.* Projected future changes in tropical cyclones using the CMIP6 HighResMIP multimodel ensemble. *Geophys. Res. Lett.* **47**, e2020GL088662 (2020).

17. Sobel, A. H. *et al.* Tropical cyclone frequency. *Earths Future* **9**, e2021EF002275 (2021).

18. Shaw, T. *et al.* Storm track processes and the opposing influences of climate change. *Nat. Geosci.* **9**, 656–664 (2016).

19. Resio, D. T. & Westerink, J. J. Modeling the physics of storm surges. *Phys. Today* **61**, 33–38 (2008).

20. Vousdoukas, M. I. *et al.* Global probabilistic projections of extreme sea levels show intensification of coastal flood hazard. *Nat. Commun.* **9**, 2360 (2018).

21. Tebaldi, C. *et al.* Extreme sea levels at different global warming levels. *Nat. Clim. Change* **11**, 746–751 (2021).

22. Taherkhani, M. *et al.* Sea-level rise exponentially increases coastal flood frequency. *Sci. Rep.* **10**, 1–17 (2020).

23. Boumis, G., Moftakhari, H. R. & Moradkhani, H. Coevolution of extreme sea levels and sea-level rise under global warming. *Earths Future* **11**, e2023EF003649 (2023).

24. Frederikse, T. *et al.* Antarctic Ice Sheet and emission scenario controls on 21st-century extreme sea-level changes. *Nat. Commun.* **11**, 390 (2020).

25. Vitousek, S. *et al.* Doubling of coastal flooding frequency within decades due to sea-level rise. *Sci. Rep.* **7**, 1399 (2017).

26. Lin, N., Marsooli, R. & Colle, B. A. Storm surge return levels induced by mid-to-late-twenty-first-century extratropical cyclones in the Northeastern United States. *Clim. Change* **154**, 143–158 (2019).

27. Marsooli, R., Lin, N., Emanuel, K. & Feng, K. Climate change exacerbates hurricane flood hazards along US Atlantic and Gulf Coasts in spatially varying patterns. *Nat. Commun.* **10**, 3785 (2019).

28. Colberg, F., McInnes, K. L., O'Grady, J. & Hoeke, R. Atmospheric circulation changes and their impact on extreme sea levels around Australia. *Nat. Hazards Earth Syst. Sci.* **19**, 1067–1086 (2019).

29. Garner, A. J. *et al.* Impact of climate change on New York City's coastal flood hazard: Increasing flood heights from the preindustrial to 2300 CE. *Proc. Natl. Acad. Sci.* **114**, 11861–11866 (2017).

30. Howard, T., Palmer, M. D. & Bricheno, L. M. Contributions to 21st century projections of extreme sea-level change around the UK. *Environ. Res. Commun.* **1**, 095002 (2019).

31. Coles, S., Bawa, J., Trenner, L. & Dorazio, P. *An Introduction to Statistical Modeling of Extreme Values*. vol. 208 (Springer, 2001).

32. Mentaschi, L. *et al.* Non-stationary extreme value analysis: a simplified approach for Earth science applications. *Hydrol Earth Syst Sci Discuss* **2016**, 1–38 (2016).

33. Marcos, M. & Woodworth, P. L. Spatiotemporal changes in extreme sea levels along the coasts of the N orth A tlantic and the G ulf of M exico. *J. Geophys. Res. Oceans* **122**, 7031–7048 (2017).

34. Baldan, D. *et al.* Importance of non-stationary analysis for assessing extreme sea levels under sea level rise. *Nat. Hazards Earth Syst. Sci.* **22**, 3663–3677 (2022).

35. Wong, T. E. An integration and assessment of multiple covariates of nonstationary storm surge statistical behavior by Bayesian model averaging. *Adv. Stat. Climatol. Meteorol. Oceanogr.* **4**, 53–63 (2018).

36. Falasca, F. *et al.* Exploring the nonstationarity of coastal sea level probability distributions. *Environ. Data Sci.* **2**, e16 (2023).

37. Calafat, F. M., Wahl, T., Tadesse, M. G. & Sparrow, S. N. Trends in Europe storm surge extremes match the rate of sea-level rise. *Nature* **603**, 841–845 (2022).

38. Roberts, M. J. *et al.* Impact of model resolution on tropical cyclone simulation using the HighResMIP–PRIMAVERA multimodel ensemble. *J. Clim.* **33**, 2557–2583 (2020).

39. Priestley, M. D. & Catto, J. L. Improved representation of extratropical cyclone structure in HighResMIP models. *Geophys. Res. Lett.* **49**, e2021GL096708 (2022).

40. Yin, J., Griffies, S. M., Winton, M., Zhao, M. & Zanna, L. Response of storm-related extreme sea level along the US Atlantic coast to combined weather and climate forcing. *J. Clim.* **33**, 3745–3769 (2020).

41. Meehl, G. A. *et al.* Effects of model resolution, physics, and coupling on Southern Hemisphere storm tracks in CESM1. 3. *Geophys. Res. Lett.* **46**, 12408–12416 (2019).

42. Chang, P. *et al.* An Unprecedented Set of High-Resolution Earth System Simulations for Understanding Multiscale Interactions in Climate Variability and Change. *J. Adv. Model. Earth Syst.* **12**, e2020MS002298 (2020).

43. Small, R. J. *et al.* A new synoptic scale resolving global climate simulation using the Community Earth System Model. *J. Adv. Model. Earth Syst.* **6**, 1065–1094 (2014).

44. Chang, P. *et al.* Uncertain future of sustainable fisheries environment in eastern boundary upwelling zones under climate change. *Commun. Earth Environ.* **4**, 19 (2023).

45. Xu, G. *et al.* High-resolution modelling identifies the Bering Strait's role in amplified Arctic warming. *Nat. Clim. Change* **14**, 615–622 (2024).

46. Ponte, R. M. Low-frequency sea level variability and the inverted barometer effect. *J. Atmospheric Ocean. Technol.* **23**, 619–629 (2006).

47. Hurricane Return Periods, National Hurricane Center and Central Pacific Hurricane Center. https://www.nhc.noaa.gov/climo/.

48. Buchanan, M. K., Oppenheimer, M. & Kopp, R. E. Amplification of flood frequencies with local sea level rise and emerging flood regimes. *Environ. Res. Lett.* **12**, 064009 (2017).

49. Ezer, T. Analysis of the changing patterns of seasonal flooding along the US East Coast. *Ocean Dyn.* **70**, 241–255 (2020).

50. Lin, N., Emanuel, K. A., Smith, J. A. & Vanmarcke, E. Risk assessment of hurricane storm surge for New York City. *J. Geophys. Res. Atmospheres* **115**, (2010).

51. Needham, H. F. & Keim, B. D. Correlating storm surge heights with tropical cyclone winds at and before landfall. *Earth Interact.* **18**, 1–26 (2014).

52. Lockwood, J. W., Lin, N., Oppenheimer, M. & Lai, C. Using neural networks to predict hurricane storm surge and to assess the sensitivity of surge to storm characteristics. *J. Geophys. Res. Atmospheres* **127**, e2022JD037617 (2022).

53. Irish, J. L., Resio, D. T. & Ratcliff, J. J. The influence of storm size on hurricane surge. *J. Phys. Oceanogr.* **38**, 2003–2013 (2008).

54. Lopez, H. *et al.* Projected increase in the frequency of extremely active Atlantic hurricane seasons. *Sci. Adv.* **10**, eadq7856 (2024).

55. Catalano, A. J. & Broccoli, A. J. Synoptic characteristics of surge-producing extratropical cyclones along the northeast coast of the United States. *J. Appl. Meteorol. Climatol.* **57**, 171–184 (2018).

56. Chang, E. K.-M. CMIP5 projected change in Northern Hemisphere winter cyclones with associated extreme winds. *J. Clim.* **31**, 6527–6542 (2018).

57. Zappa, G., Shaffrey, L. C., Hodges, K. I., Sansom, P. G. & Stephenson, D. B. A multimodel assessment of future projections of North Atlantic and European extratropical cyclones in the CMIP5 climate models. *J. Clim.* **26**, 5846–5862 (2013).

58. Seiler, C. & Zwiers, F. W. How will climate change affect explosive cyclones in the extratropics of the Northern Hemisphere? *Clim. Dyn.* **46**, 3633–3644 (2016).

59. Wang, J., Kim, H.-M. & Chang, E. K. Changes in Northern Hemisphere winter storm tracks under the background of Arctic amplification. *J. Clim.* **30**, 3705–3724 (2017).

60. Haarsma, R. J. *et al.* High resolution model intercomparison project (HighResMIP v1. 0) for CMIP6. *Geosci. Model Dev.* **9**, 4185–4208 (2016).

61. Roberts, M. J. *et al.* High-Resolution Model Intercomparison Project phase 2 (HighResMIP2) towards CMIP7. *Geosci. Model Dev.* **18**, 1307–1332 (2025).

62. Caldwell, P., Merrifield, M. & Thompson, P. Sea level measured by tide gauges from global oceans–the Joint Archive for Sea Level holdings (NCEI Accession 0019568), Version 5.5, NOAA National Centers for Environmental Information, Dataset. *Cent. Env. Inf. Dataset* **10**, V5V40S7W (2015).

63. Haigh, I. D. *et al.* GESLA version 3: A major update to the global higher-frequency sea-level dataset. *Geosci. Data J.* **10**, 293–314 (2023).

64. Woodworth, P. L. *et al.* Towards a global higher-frequency sea level dataset. *Geosci. Data J.* **3**, 50–59 (2016).

65. Codiga, D. UTide unified tidal analysis and prediction functions. *MATLAB Cent. File Exch.* (2020).

66. Dangendorf, S. *et al.* Acceleration of US Southeast and Gulf coast sea-level rise amplified by internal climate variability. *Nat. Commun.* **14**, 1935 (2023).

67. Dangendorf, S. *et al.* Probabilistic reconstruction of sea-level changes and their causes since 1900. *Earth Syst. Sci. Data Discuss.* **2024**, 1–37 (2024).

68. Hersbach, H. *et al.* ERA5 hourly data on single levels from 1940 to present. Copernicus Climate Change Service (C3S) Climate Data Store (CDS). https://doi.org/10.24381/cds.adbb2d47 (2023).

Extended Figures

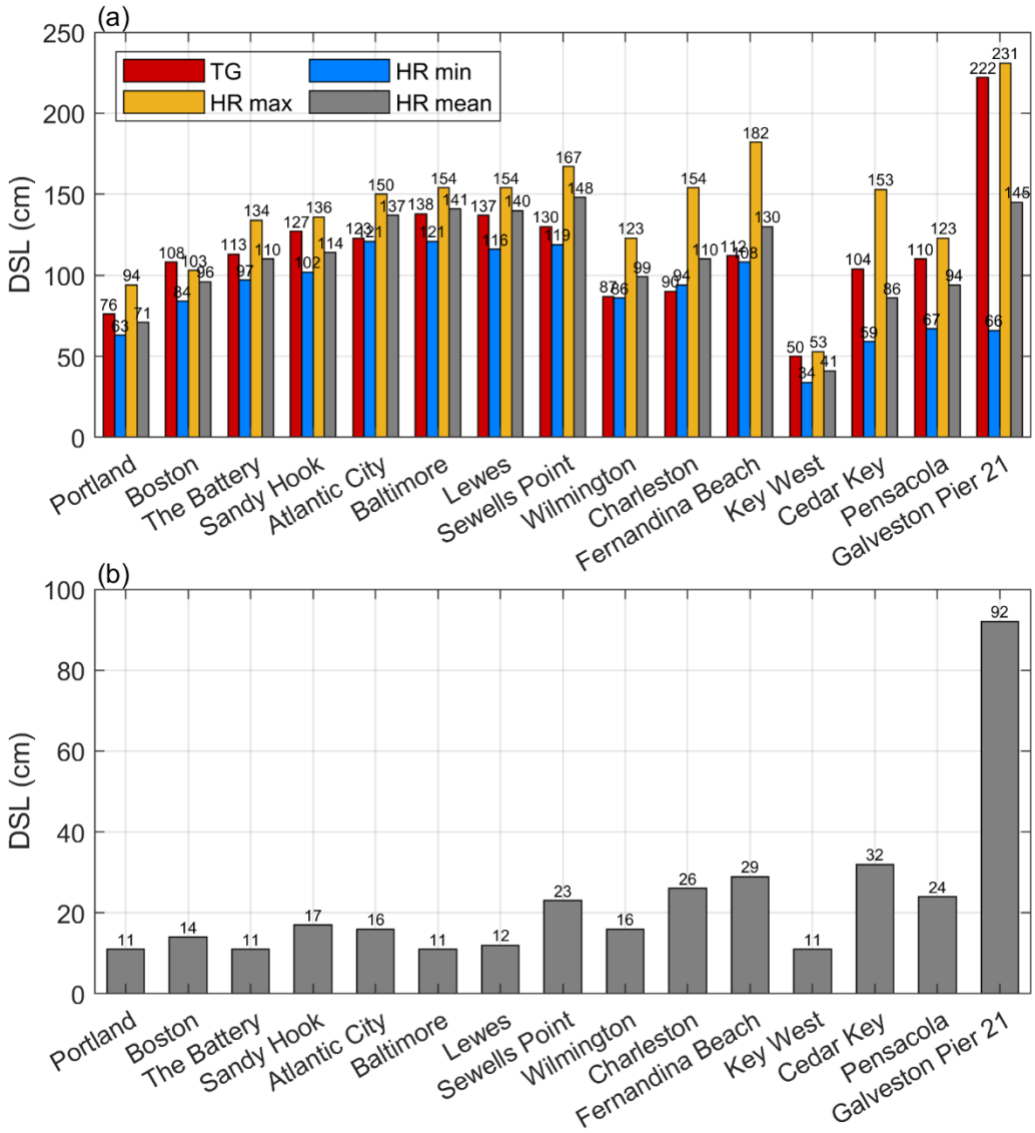

Extended Figure 1 Uncertainties in maximum DSL in HR CESM. (a) Comparison of maximum DSL from TG observations (red) with the ensemble minima (blue), maxima (yellow), and mean (gray) of maximum DSL values across 10 HR CESM ensemble members at 15 TG stations. (b) RMSE of the maximum DSL in HR CESM.

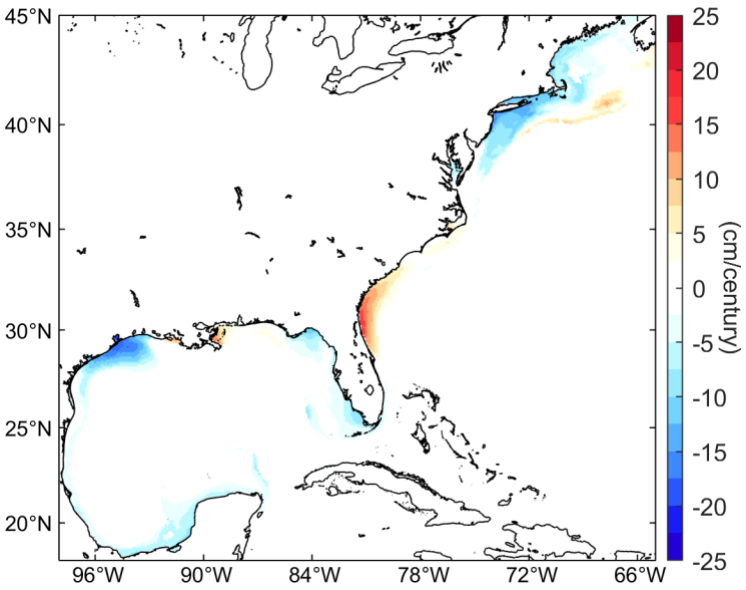

Extended Figure 2 DSL50 trends in HR CESM. ensemble-mean DSL50 trends in leave-one-out analysis from 2006 to 2100.

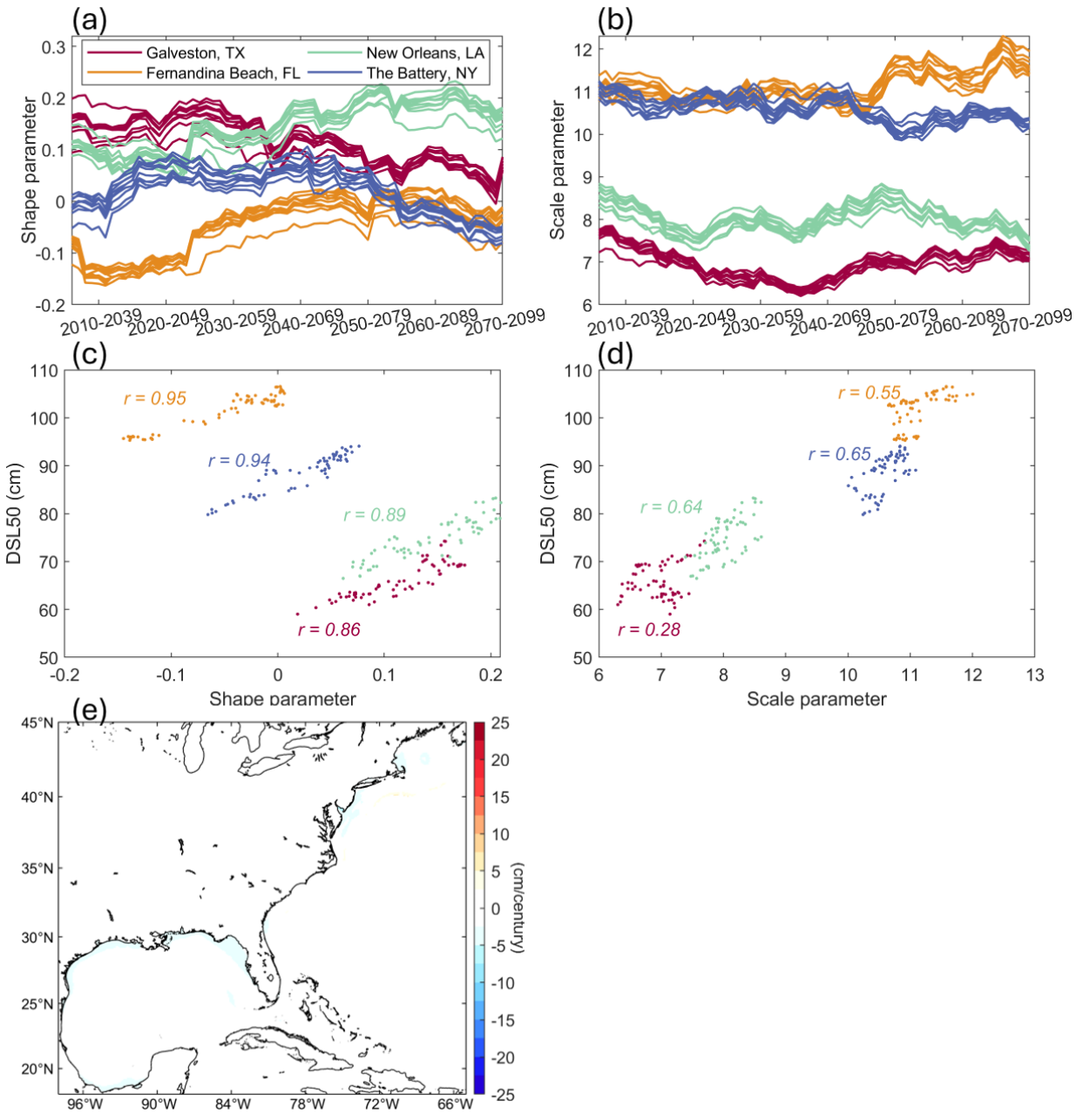

Extended Figure 3 Relationship between GEV parameters and wind-induced DSL50 trends. (a, b) Time series of (a) shape and (b) scale parameters of GEV distributions using 9 out of 10 ensemble members. (c, d) Scatterplot of wind-induced DSL50 versus **(c)** shape and **(d)** scale parameters using 10 ensemble members. The correlation coefficients between wind-

induced DSL50 and these two parameters are indicated in each panel. **(e)** Contributions of the location parameter to the wind-induced DSL50 trend using 10 ensemble members.

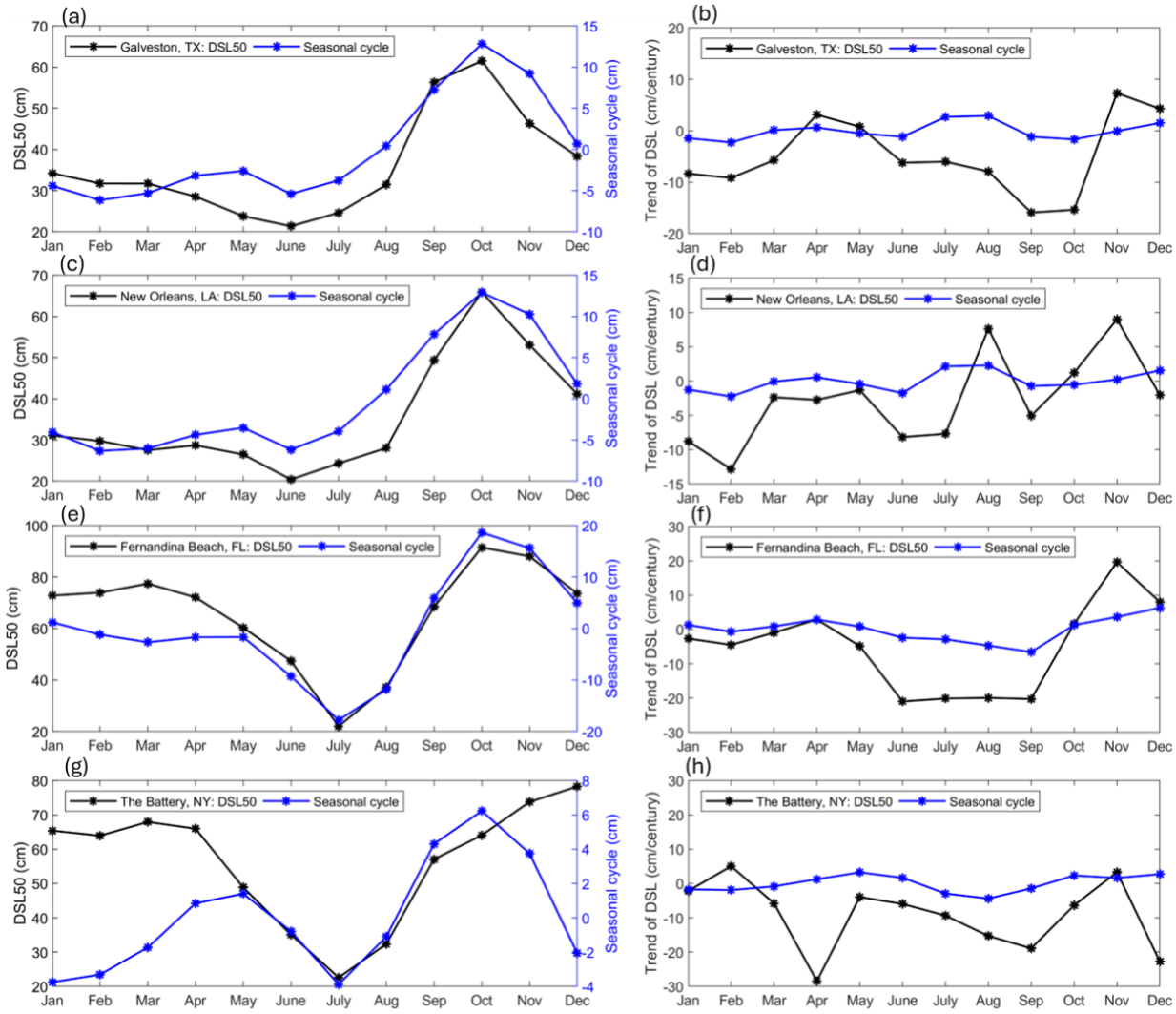

Extended Figure 4 Seasonal trends in DSL50 and mean DSL from 2006 to 2100. (a, c, e, g) Seasonal cycles of DSL (blue) and DSL50 (black) averaged over 2006-2035. (b, d, f, h) Trends in seasonal cycles of DSL (blue) and DSL50 (black) from 2006 to 2100.

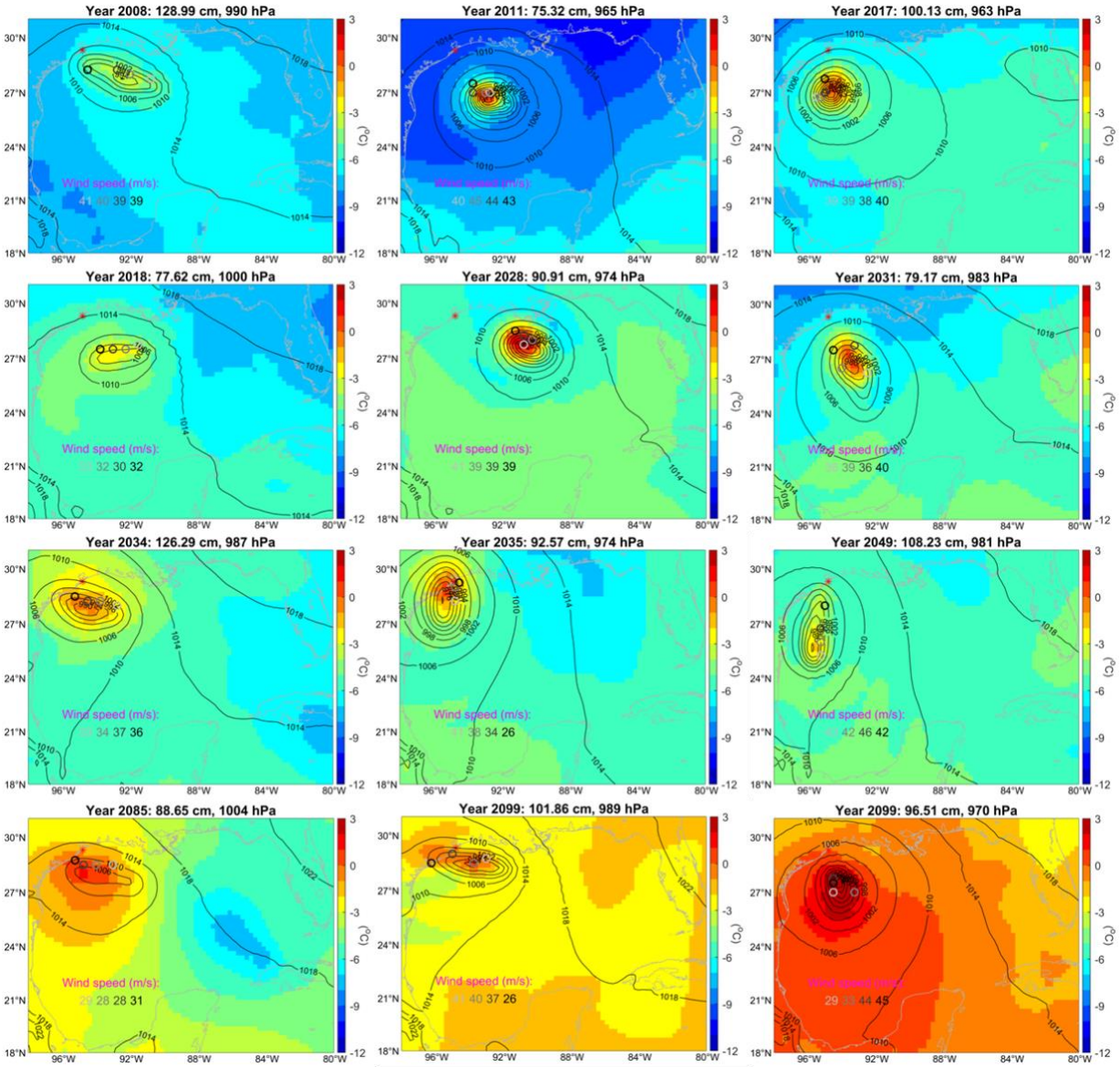

Extended Figure 5 Severe events for Galveston in HR CESM. Each panel displays the time, DSL, and minimum SLP as indicated in the panel titles. Color shading represents the daily mean air temperature at 500 hPa, while contours indicate the daily mean SLP. The 6-hourly surface wind speeds are shown in the lower-left corner of each panel, with darker colors indicating later times.

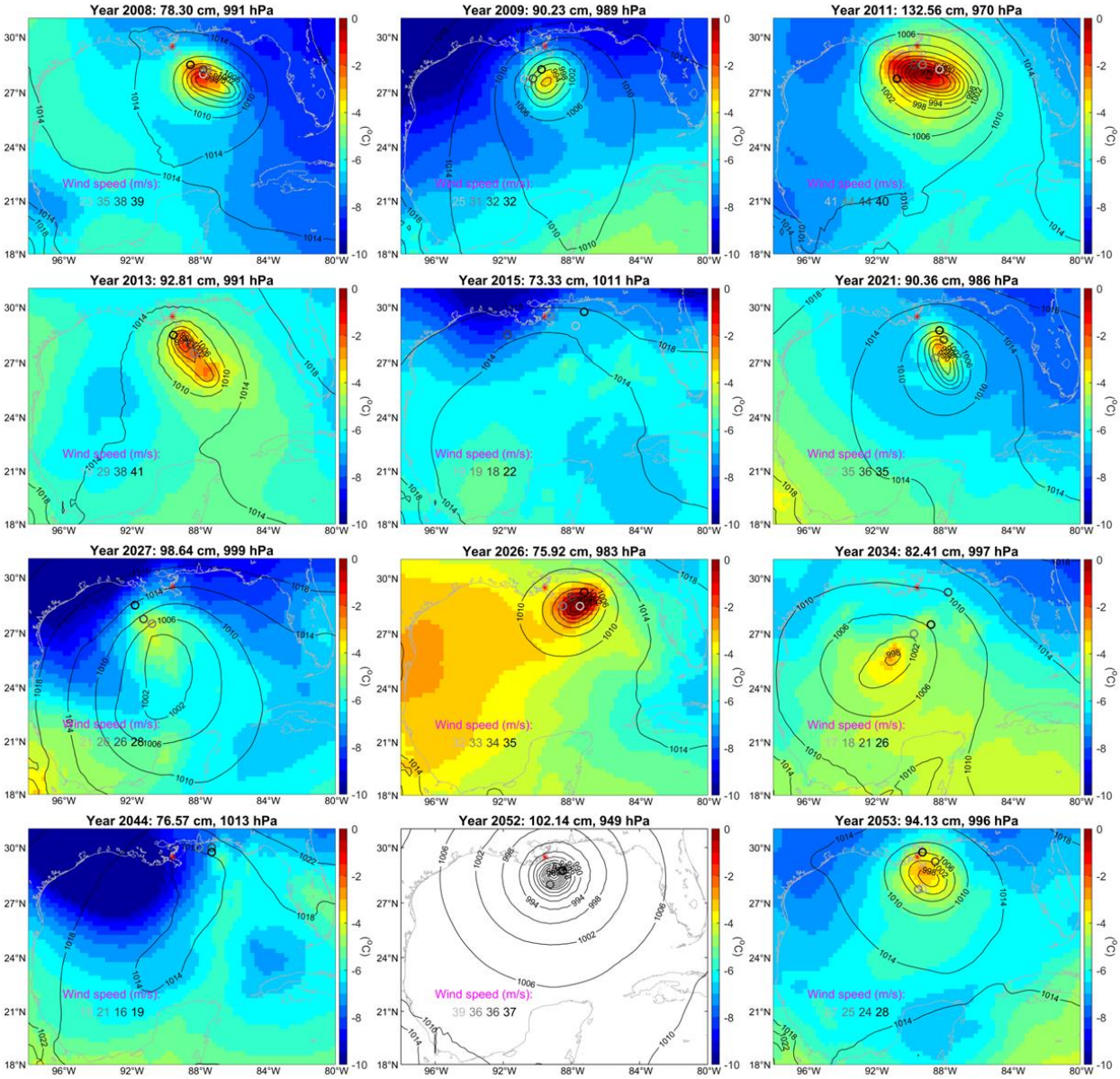
Year 2008: 78.30 cm, 991 hPa
Wind speed (m/s):
33 35 38 39
Year 2009: 90.23 cm, 989 hPa
Wind speed (m/s):
25 31 32 32
Year 2011: 132.56 cm, 970 hPa
Wind speed (m/s):
41 44 44 40
Year 2013: 92.81 cm, 991 hPa
Wind speed (m/s):
29 38 41
Year 2015: 73.33 cm, 1011 hPa
Wind speed (m/s):
19 18 22
Year 2021: 90.36 cm, 986 hPa
Wind speed (m/s):
35 36 35
Year 2027: 98.64 cm, 999 hPa
Wind speed (m/s):
25 26 26 28
Year 2026: 75.92 cm, 983 hPa
Wind speed (m/s):
33 33 34 35
Year 2034: 82.41 cm, 997 hPa
Wind speed (m/s):
17 18 21 26
Year 2044: 76.57 cm, 1013 hPa
Wind speed (m/s):
21 21 16 19
Year 2052: 102.14 cm, 949 hPa
Wind speed (m/s):
39 36 36 37
Year 2053: 94.13 cm, 996 hPa
Wind speed (m/s):
27 25 24 28
30°N
27°N
24°N
21°N
18°N
96°W
92°W
88°W
84°W
80°W
(°C)

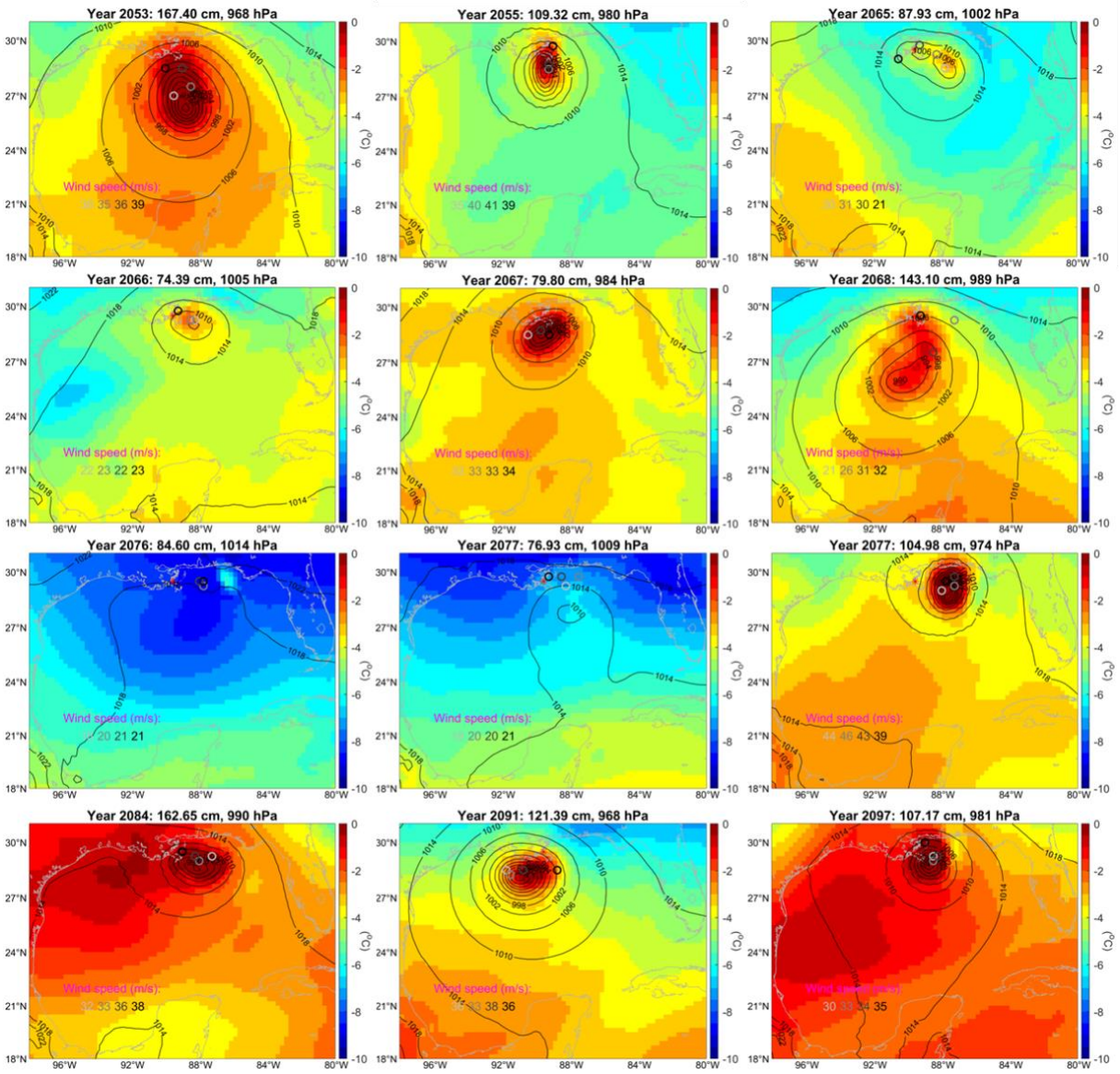

Extended Figure 6 Severe events for New Orleans in HR CESM. Each panel displays the time, DSL, and minimum SLP as indicated in the panel titles. Color shading represents the daily mean air temperature at 500 hPa, while contours indicate the daily mean SLP. The 6-hourly surface wind speeds are shown in the lower-left corner of each panel, with darker colors indicating later times.

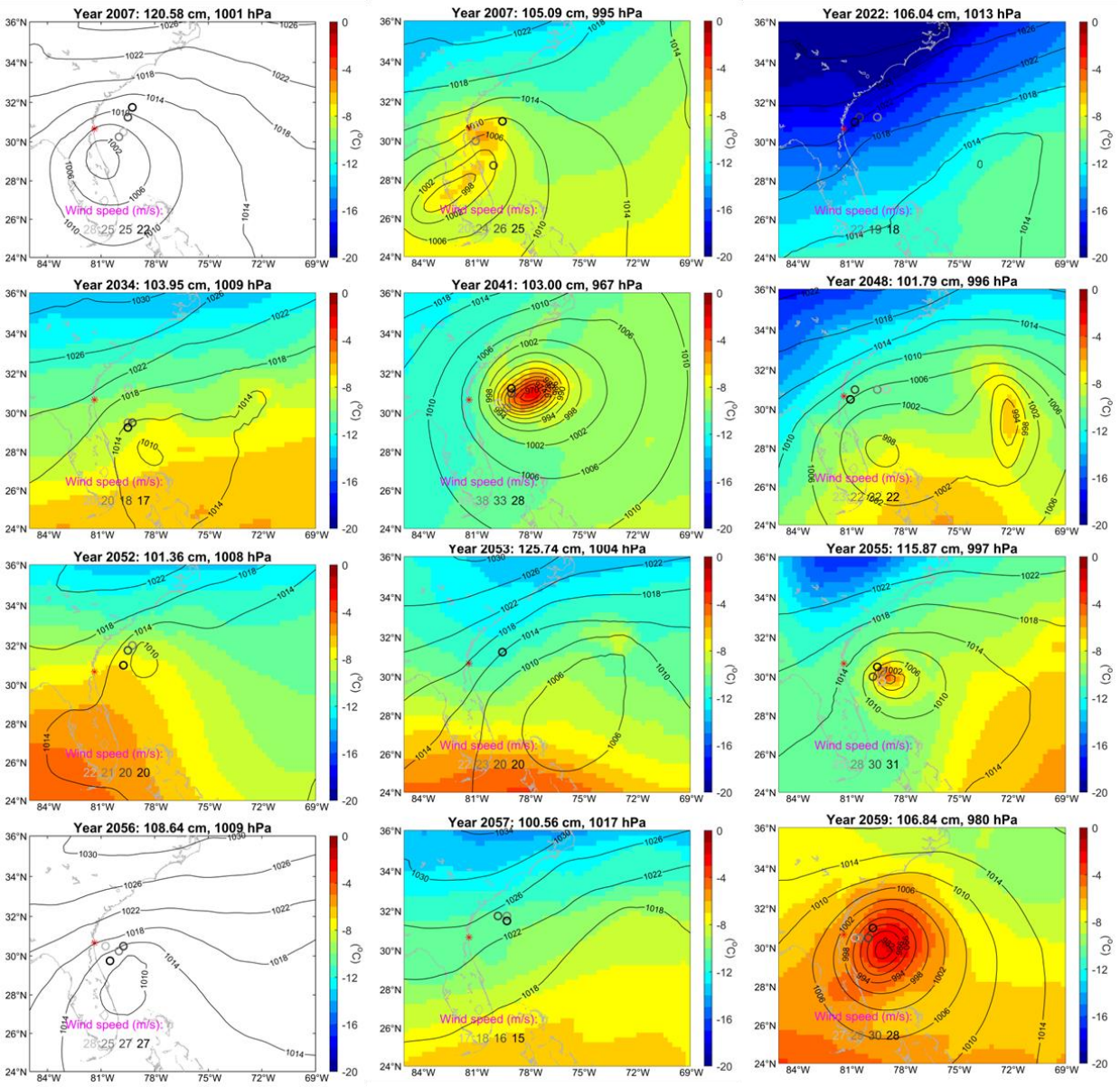
Year 2007: 120.58 cm, 1001 hPa
Wind speed (m/s):
28 25 25 22
Year 2007: 105.09 cm, 995 hPa
Wind speed (m/s):
34 26 25
Year 2022: 106.04 cm, 1013 hPa
Wind speed (m/s):
22 19 18
Year 2034: 103.95 cm, 1009 hPa
Wind speed (m/s):
20 18 17
Year 2041: 103.00 cm, 967 hPa
Wind speed (m/s):
38 33 28
Year 2048: 101.79 cm, 996 hPa
Wind speed (m/s):
22 22 22
Year 2052: 101.36 cm, 1008 hPa
Wind speed (m/s):
22 21 20 20
Year 2053: 125.74 cm, 1004 hPa
Wind speed (m/s):
23 20 20
Year 2055: 115.87 cm, 997 hPa
Wind speed (m/s):
28 30 31
Year 2056: 108.64 cm, 1009 hPa
Wind speed (m/s):
28 25 27 27
Year 2057: 100.56 cm, 1017 hPa
Wind speed (m/s):
17 18 16 15
Year 2059: 106.84 cm, 980 hPa
Wind speed (m/s):
27 29 30 28
(°C)

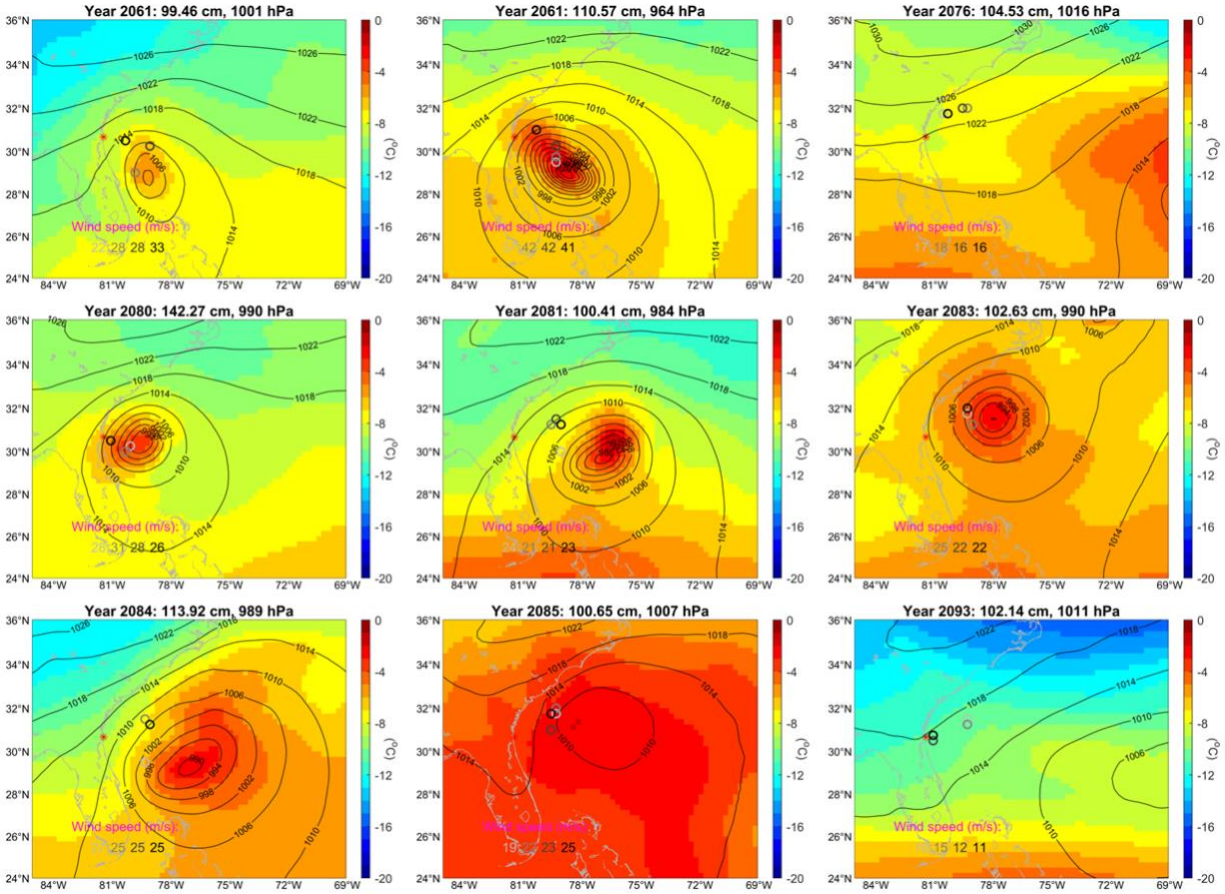

Extended Figure 7 Severe events for Fernandina Beach in HR CESM. Each panel displays the time, DSL, and minimum SLP as indicated in the panel titles. Color shading represents the daily mean air temperature at 500 hPa, while contours indicate the daily mean SLP. The 6-hourly surface wind speeds are shown in the lower-left corner of each panel, with darker colors indicating later times.

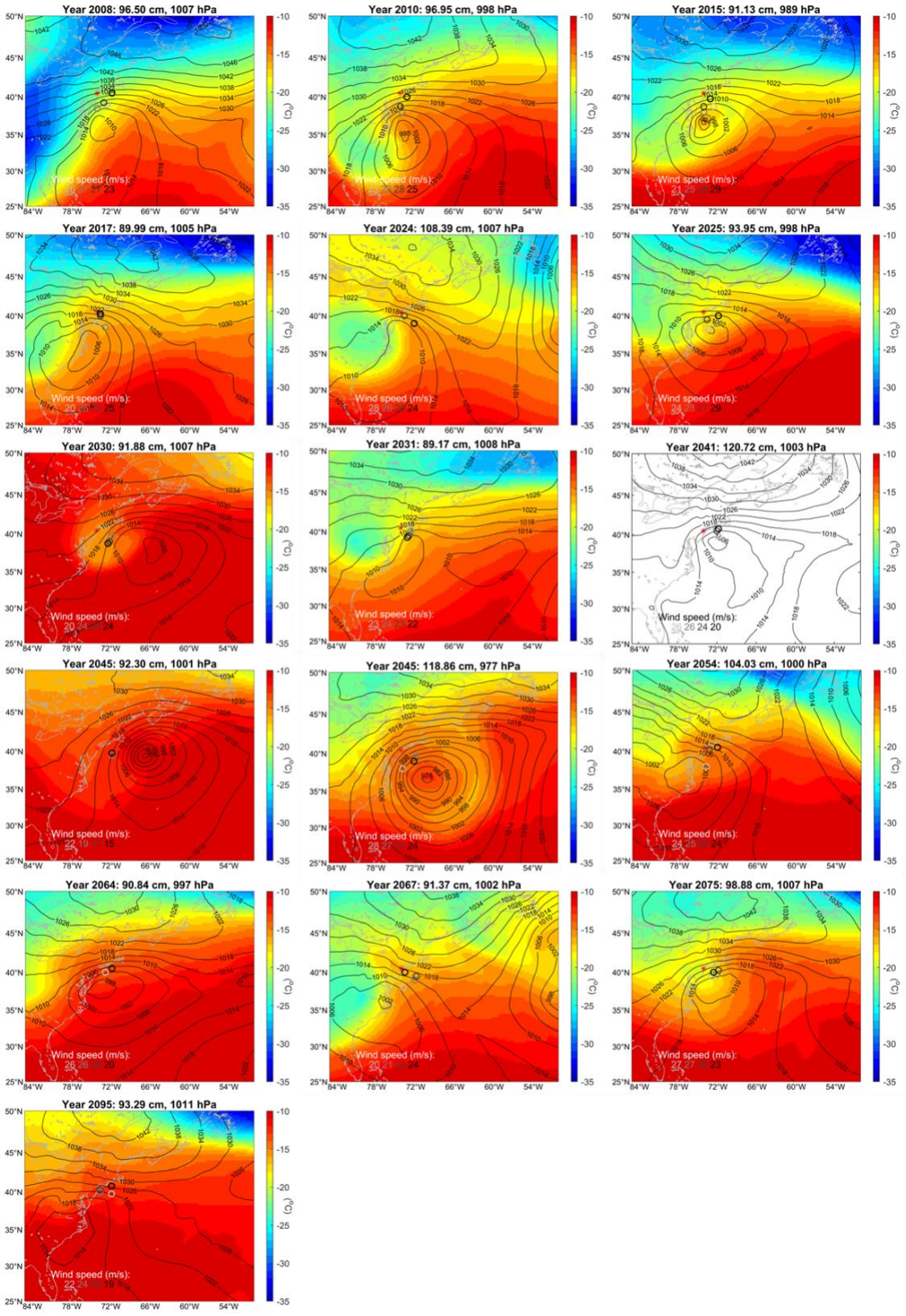
Year 2008: 96.50 cm, 1007 hPa
Year 2010: 96.95 cm, 998 hPa
Year 2015: 91.13 cm, 989 hPa
Year 2017: 89.99 cm, 1005 hPa
Year 2024: 108.39 cm, 1007 hPa
Year 2025: 93.95 cm, 998 hPa
Year 2030: 91.88 cm, 1007 hPa
Year 2031: 89.17 cm, 1008 hPa
Year 2041: 120.72 cm, 1003 hPa
Year 2045: 92.30 cm, 1001 hPa
Year 2045: 118.86 cm, 977 hPa
Year 2054: 104.03 cm, 1000 hPa
Year 2064: 90.84 cm, 997 hPa
Year 2067: 91.37 cm, 1002 hPa
Year 2075: 98.88 cm, 1007 hPa
Year 2095: 93.29 cm, 1011 hPa
Wind speed (m/s):
50°N
45°N
40°N
35°N
30°N
25°N
84°W
78°W
72°W
66°W
60°W
54°W
(°C)

Extended Figure 8 Severe events for The Battery in HR CESM. Each panel displays the time, DSL, and minimum SLP as indicated in the panel titles. Color shading represents the daily mean air temperature at 500 hPa, while contours indicate the daily mean SLP. The 6-hourly surface wind speeds are shown in the lower-left corner of each panel, with darker colors indicating later times.